Powder metallurgy processing of seven/eight component multi-phase (HfTiZr-Mn/Mo/W/Cr/Ta)B$_2$ high entropy diboride ceramics

İlayda Süzer [a,*], Amir Akbari [a], Semih Ates [b], Kübra Gürcan Bayrak [c], Sıddıka Mertdinç-Ülküseven [a], C. Fahir Arisoy [b], M. Lütfi Öveçoğlu [a,d], Duygu Ağaoğulları [a,**]

[a] *Istanbul Technical University, Faculty of Chemical and Metallurgical Engineering, Department of Metallurgical and Materials Engineering, Particulate Materials Laboratories (PML), Graphene & 2D Materials Laboratory, 34469, Maslak, Istanbul, Turkiye*
[b] *Istanbul Technical University, Faculty of Chemical and Metallurgical Engineering, Department of Metallurgical and Materials Engineering, 34469, Maslak, Istanbul, Turkiye*
[c] *Eskişehir Technical University, Faculty of Engineering, Department of Materials Science and Engineering, İki Eylül Campus, 26555, Eskişehir, Turkiye*
[d] *MEF University, Department of Mechanical Engineering, 34396, Sarıyer, Istanbul, Turkiye*

ARTICLE INFO

ABSTRACT

This study aims to show the possibility of synthesizing seven- and eight-component high entropy diboride (HEB) ceramics using high energy ball milling-assisted spark plasma sintering (SPS). Metal boride powders, synthesized in laboratory conditions from metal oxide-boron oxide-magnesium powder blends, were combined equimolarly as seven and eight components containing systems. Afterwards, hybridized powders were mechanically alloyed (MA) for 6 h and subjected to spark plasma sintering (SPS) at 2000 °C and under 30 MPa. Detailed phase analysis and physical, microstructural, and mechanical characterization of the samples were performed. ın the sintered products, the main phase belongs to the HEB, and also low amounts of Hf/Zr oxides and secondary phases (W or Ti-rich) occurred. The highest hardness was observed at the (HfTiZrMoWCrTa)B$_2$ with ~25 GPa, and the lowest hardness was seen at the (HfTiZrMnCrMoWTa)B$_2$ with ~17 GPa. Also, the highest wear resistance was calculated for the (HfTiZrMnCrMoTa)B$_2$ as 6.05×10^{-7} mm^3/Nm. Additionally, (HfTiZrMnMoWTa)B$_2$ and (HfTiZrMn-MoCrTa)B$_2$ have the highest and lowest Archimedes' densities, with 7.94 g/cm^3 and 6.91 g/cm^3, respectively.

1. Introduction

Transition metal borides are a subgroup of advanced ceramics [1]. They have different crystal structures and superior properties [2], characterized by high melting temperature, good thermal conductivity, low density, high hardness, and wear resistance thanks to strong ionic and covalent bonds [3–6]. With all these features, borides are combined to form different alloy groups rather than being used monolithically one. Especially in the last 20 years, new alloy groups with more advanced properties, single phase, and containing three or more elements have also been identified as high entropy alloys (HEA). HEAs with advanced and superior properties were first defined in 2004 [7,8]. According to the element-based definition, HEA comprises four or more elements in an equimolar ratio [7]. The configurational entropy (ΔS_{conf}) is greater than or equal to 1.61R ($\Delta S_{conf} \geq 1.61R$; R is the gas constant) [9,10]. Although a HEA contains more than four elements, it has a single-phase structure [11]. The formation of solid solutions and four different core effects (high entropy, sluggish diffusion, severe-lattice distortion, and cocktail effect) cause single-phase [12,13]. There are many studies describing the formation of HEAs. Moreover, more than four hundred HEAs have been developed by 2021 [13]. Today, however, it is noticed that high-entropy alloys extend with the studies of high entropy nitride [14], oxide [15], boride [16,17], carbide [18], sulfide [19,20], and silicide [21]. Among these ceramics, high entropy boride ceramics have become a very interesting topic for the last eight years, and numerous studies have been completed.

Gild et al. [22] identified high entropy metal boride ceramics (HEBs) in 2016. Like HEAs, HEB ceramics have a single-phase structure, although they contain multiple components. However, HEBs have a hexagonal close-packed structure with AlB$_2$ type and highly anisotropic layers [23,24]. Similar to the HEAs, HEBs have superior features: high hardness, elastic modulus, and wear resistance due to solid-solution

---

* Corresponding author.
** Corresponding author.
  E-mail addresses: suzeri@itu.edu.tr (İ. Süzer), bozkurtdu@itu.edu.tr (D. Ağaoğulları).

hardening [24]. Moreover, they have good electrical conductivities and stronger electron and phonon scattering than monolithic diborides [25]. Additionally, HEB ceramics have high room-temperature resistivities, thermal conductivity, and high melting points [26,27]. These properties significantly improve compared to traditional binary boride alloys or transition metal borides. Many methods are used in the synthesis of HEB ceramics with these superior properties. Boro/carbothermal reduction [28] and mechanical alloying [17] are often preferred when combining and blending powders. Then, spark plasma sintering (SPS) [29] is generally preferred to densify the powders. However, hot pressing can also be preferred [30]. In recent years, ultra-fast high-temperature synthesis (UHS) has also come to the fore during densification [31].

In the first HEB study conducted by Gild et al. [22], seven different compositions [$(Hf_{0.2}Zr_{0.2}Ta_{0.2}Cr_{0.2}Ti_{0.2})B_2$, $(Hf_{0.2}Zr_{0.2}Ta_{0.2}Mo_{0.2}Ti_{0.2})$ B_2, $(Hf_{0.2}Zr_{0.2}W_{0.2}Mo_{0.2}Ti_{0.2})B_2$, etc.], were produced by MA (6 h) and SPS (2000 °C, 30 MPa) using commercial starting boride powders. HEB, secondary, and oxide phases were detected. Vickers hardness measurements (200 kgf/mm^2, 15 s) yielded values between 17.5 and 24 GPa. In our previous study, Süzer et al. [16] synthesized seven different HEB ceramics [$(HfTiZr)B_2$, $(HfTiZrMnCr)B_2$, $(HfTiZrMn)B_2$, $(TiZrMnCr)B_2$, etc.], by ball milling and SPS (2000 °C, 30 MPa). We found HEB, oxide, and secondary phases. Also, $(HfTiZrMnCr)B_2$ composition has the highest hardness value (~27 GPa) and the lowest wear rate (~2×10^{-6} Nm/mm^3). The composition of $(HfTiZrMnCr)B_2$ synthesized in our previous study will be helpful for comparison in this study. Guo et al. [31] synthesized different HEB ceramics from 5 to 8 components using UHS. Secondary phases were also formed along with the HEB phases. They found the hardness values for seven [$(Ti_{0.22}Cr_{0.06}Zr_{0.17}Hf_{0.14-}$ $Ta_{0.10}Mo_{0.16}Nb_{0.16})B_2$] and eight [$(Ti_{0.19}Cr_{0.06}Zr_{0.10}Hf_{0.08}Ta_{0.06-}$ $Mo_{0.16}Nb_{0.12}V_{0.23})B_2$] component HEBs to be approximately 21 GPa and 18 GPa, respectively. Thus, it was demonstrated that synthesis can be done with 7 and 8 components in the HEB ceramics. Zhang et al. [32] synthesized $(Zr_{0.2}Ta_{0.2}Ti_{0.2}Nb_{0.2}Hf_{0.2})B_2$ and $(Zr_{0.2}W_{0.2}Ti_{0.2}Mo_{0.2}Hf_{0.2})$ B_2 ceramics by borothermal reduction and SPS (2000 °C). They also encountered secondary phases in the composition containing W boride. Again, the W boride composition has a hardness of approximately 27 GPa. In this way, a comparison can be made with compositions containing W-boride. When all studies are examined, compounds such as HfB_2, TiB_2, ZrB_2, TB_2 and VB_2, and NbB_2 have been widely used in the synthesis of HEB ceramics since 2016 [33–39]. In addition, various HEB compositions have been produced with CrB_2, MoB_2, and W boride (WB_2, W_2B, and WB) compounds [17,29,32,40–42]. Also, studies have shown that dual-phase or multi-phase HEB production and single-phase HEB synthesis occur [17,22,43]. However, there is one study involving Mn boride [16]. To the best of our knowledge, there is no study in which all these common elements are used together.

In this study, it has been shown that seven and eight-component HEB ceramics can be synthesized via high-energy ball milling-assisted spark plasma sintering. HEB studies in the literature so far have primarily focused on five components [22,32,38,44–46]. Moreover, compositions containing three [47,48], four [27,49], and six components [50] have also been synthesized. In addition, Yeh [51] has calculated configurational entropy for up to thirteen elements in high entropy alloys when accounting for core effects. As a result of the calculations, they predicted that the high entropy effect began to decrease in HEAs produced after eleven elements. Therefore, the effect of increasing the number of components can also be observed in a high entropy system. Apart from this, only one study includes seven component HEBs with UHS [31]. To the best our knowledge, no seven- or eight-component systems are produced with high-energy ball milling and SPS. The starting boride powders used in this study were synthesized in our laboratory facilities and seven/eight component containing HEB ceramics were constituted. The study with these values contributes significantly to the current literature.

2. Experimental procedure

2.1. Synthesis of the HEB ceramics

Borides (HfB_2, TiB_2, ZrB_2, TaB, Mn boride, Cr boride, W boride, Mo boride) as starting powders were synthesized by mechanochemical synthesis (MCS) and leaching process by choosing the optimum parameters under laboratory conditions. Previous studies [16,17] defined optimum conditions for synthesizing different borides (HfB_2, TiB_2, ZrB_2, W boride, Mn boride, and Cr boride). The synthesized borides were prepared in equimolar ratios to 7 or 8 components over 6 g. The amounts of powder for production were calculated based on the states where the compounds are considered to be stable (HfB_2, TiB_2, ZrB_2, MnB_2, MoB_2, CrB_2, W_2B, and TaB). On the other hand, elemental boron (B, Pavtec, in purity >99 %, particle size <400 nm) was added to provide diboride stoichiometry. The starting materials and their corresponding amounts used in the experimental procedure for each composition are shown in Table S.1. The amounts of powder used in the experimental procedure as starting material are given in detail in Table S1. Sample codes of the prepared compositions are given in Table 1. The compound $(HfTiZr)B_2$ is called as HEB. Other borides were added to the composition and shown in the sample code section. The production of the HEB composition was described in our previous work [16].

The compositions were mixed in a turbula blender (WAB T2C) for 2 h. Then, the blended powders were placed in WC vials (50 ml) and balls (Ø 6 mm) in a glovebox (MBRAUN) under an Argon (Linde, 99.99 % purity) atmosphere. The 10:1 was chosen as the ball-to-powder weight ratio (BPR). The placed powders were milled in a Spex 8000D Mixer/ Mill for 6 h. The milled powders were sintered in an SPS furnace (HPD-50, FCT GmbH, Germany) with a 10^{-2} mbar vacuum environment. The samples were subjected to an uniaxial pressure of 30 MPa for 10 min at a sintering temperature of 2000 °C. During the sintering process, heating rate of 100 °C/min was applied until the target temperature of 2000 °C was reached. After holding at this temperature for 10 min, the heating was switched off (~500 °C/min). An optical pyrometer was used to monitor the temperature on the graphite die surface as the temperature was raised using a regulated electric current, with accurate measurements taken within the temperature range of 450–2000 °C. The schematic cycle of the SPS process is given in Fig. S1. The powders were placed into a hollow cylindrical graphite die with a diameter of 20 mm and a length of 48 mm, using graphite foil to prevent a reaction between the powders and the graphite die (Carbin Graphite & Carbon Materials). To minimize heat loss, the die was covered with two layers of graphite felt.

2.2. Characterization of the HEB ceramics

Phase analyses of both powders and sintered samples were conducted with Bruker D8 X-ray diffractometer (XRD) with CuK_α (1.5406 Å, 35 kV, 40 mA, and 0.02° step size) radiation in the 2θ range of 20–90° increments at a rate of 2°/min. Crystalline phases were determined using the powder diffraction database from the International Center for Diffraction Data® (ICDD). The densities of the average powders were measured 10 times at room temperature with a Micromeritics AccuPyc-II 1340 Helium-gas pycnometer. The sintered samples were mounted,

Table 1
Sample codes and their corresponding compositions.

Composition	Sample Code
$(Hf_{0.125}Ti_{0.125}Zr_{0.125}Mn_{0.125}Mo_{0.125}W_{0.125}Cr_{0.125}Ta_{0.125})B_2$	HEB/MnMoWCrTa
$(Hf_{0.143}Ti_{0.143}Zr_{0.143}Mo_{0.143}W_{0.143}Mn_{0.143}Cr_{0.143})B_2$	HEB/MnMoWCr
$(Hf_{0.143}Ti_{0.143}Zr_{0.143}Mo_{0.143}Ta_{0.143}Mn_{0.143}Cr_{0.143})B_2$	HEB/MnMoCrTa
$(Hf_{0.143}Ti_{0.143}Zr_{0.143}Mo_{0.143}Ta_{0.143}W_{0.143}Mn_{0.143})B_2$	HEB/MnMoWTa
$(Hf_{0.143}Ti_{0.143}Zr_{0.143}W_{0.143}Ta_{0.143}Mn_{0.143}Cr_{0.143})B_2$	HEB/MnWCrTa
$(Hf_{0.143}Ti_{0.143}Zr_{0.143}Mo_{0.143}Ta_{0.143}W_{0.143}Cr_{0.143})B_2$	HEB/MoWCrTa

ground, and polished. The previous study explained the grinding and polishing processes in detail [16]. Sintered sample phases were analyzed in the same situations as milled powder samples. Morphological investigations were carried out with a ThermoScientific Quattro S scanning electron microscope (SEM) and energy dispersive spectrometer (EDS). The Archimedes' densities of the samples were measured in a distilled water environment after three measurements. Additionally, Vickers hardness and wear tests were done to understand mechanical behaviors. The hardness test parameters were a force of 0.9807 N (100 g) and an indentation period of 10 s at room temperature (FutureTech Microhardness Tester). Twenty-five individual measurements were taken to calculate average hardness values. A 5 mm diameter WC ball was utilized in dry sliding wear testing (Bruker Umt-2). The sliding speed, the distance, and the wear track length were 6 mm/s, 100 m, and 2 mm, respectively. The tests were conducted with a 4 N standard load at room temperature. The worn surface profiles were acquired with a Veeco Dektak 6 M Stylus profiler; the findings were presented as the mean of three individual measurements, and the wear rate was determined. A Nikon Eclipse L150 optical microscope was used to analyze the surfaces of the worn samples. A schematic diagram of the experimental procedure is given in Fig. 1.

3. Results & discussion

3.1. Characterization of the powders

Fig. 2a–f illustrates the XRD patterns of the as-blended compositions.

All compositions consist only of initial powder blends and many stoichiometric borides. Moreover, the whole composition does not contain any by-products or oxide phases. The reason for different boride compounds is that the powders are synthesized under laboratory conditions. The HfB_2 phase at approximately $2\theta = 42^o$ is the most intense peak in all compositions. Approximate peak positions of the binary boride compounds and their ICDD card numbers are also shown in Table S.2. XRD patterns after the HEBM process are shown in Fig. 2g–k. The boride phases gradually disappeared and started to form high-intensity HEB peaks. However, there are also W_2B, CrB, Mo_2B and TaB phases. This study includes a TiB_2-rich phase, similar to our previous study [16]. These phases are thought to contain more than one boride, but predominantly TiB_2. HEB formation still needs to be completed. In the studies conducted so far, there are cases where the single-phase HEB structure does not form after mechanical alloying, even during long-term milling times [17,22,42,52–54]. Additionally, low-intensity WC (ICDD No: 00-002-1055) peaks were observed in the XRD patterns of the HEB/MnMoWTa and HEB/MoWCrTa compounds. These peaks are predicted to form due to contamination of the tungsten carbide milling media. Besides all these, no secondary phase or oxide formation was found. Moreover, according to the as-blended XRD patterns (Fig. 2a–f), the broadening of the peaks began to be observed after milling. The changes during MA (decreasing crystallinity, high lattice strain, grain size reduction) cause this situation [55–57].

Table S.3 shows the average density values of the powder compositions after milling. The highest (HEB/MoWCrTa) and lowest density (HEB/MnMoCrTa) values are seen in seven-component compositions.
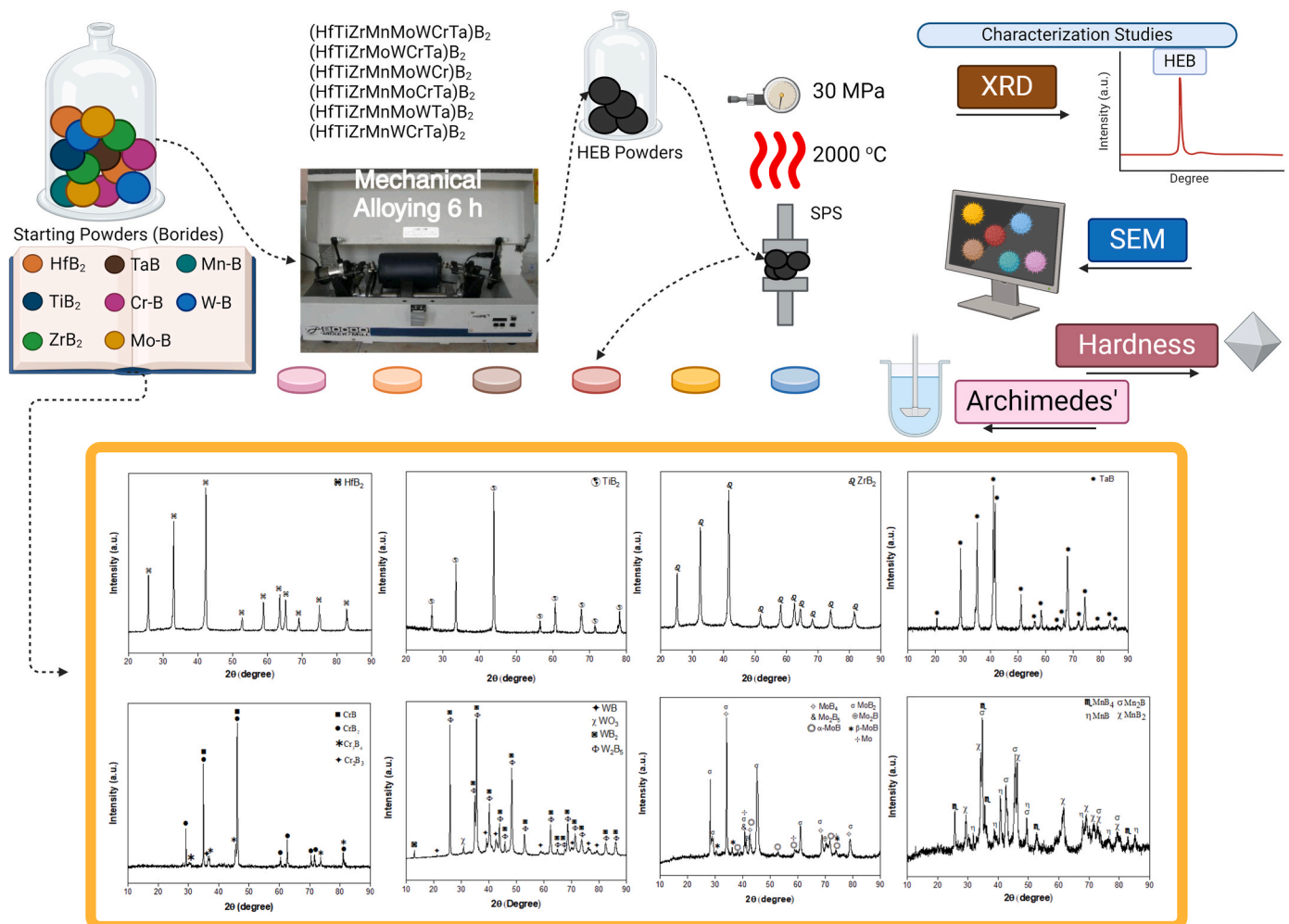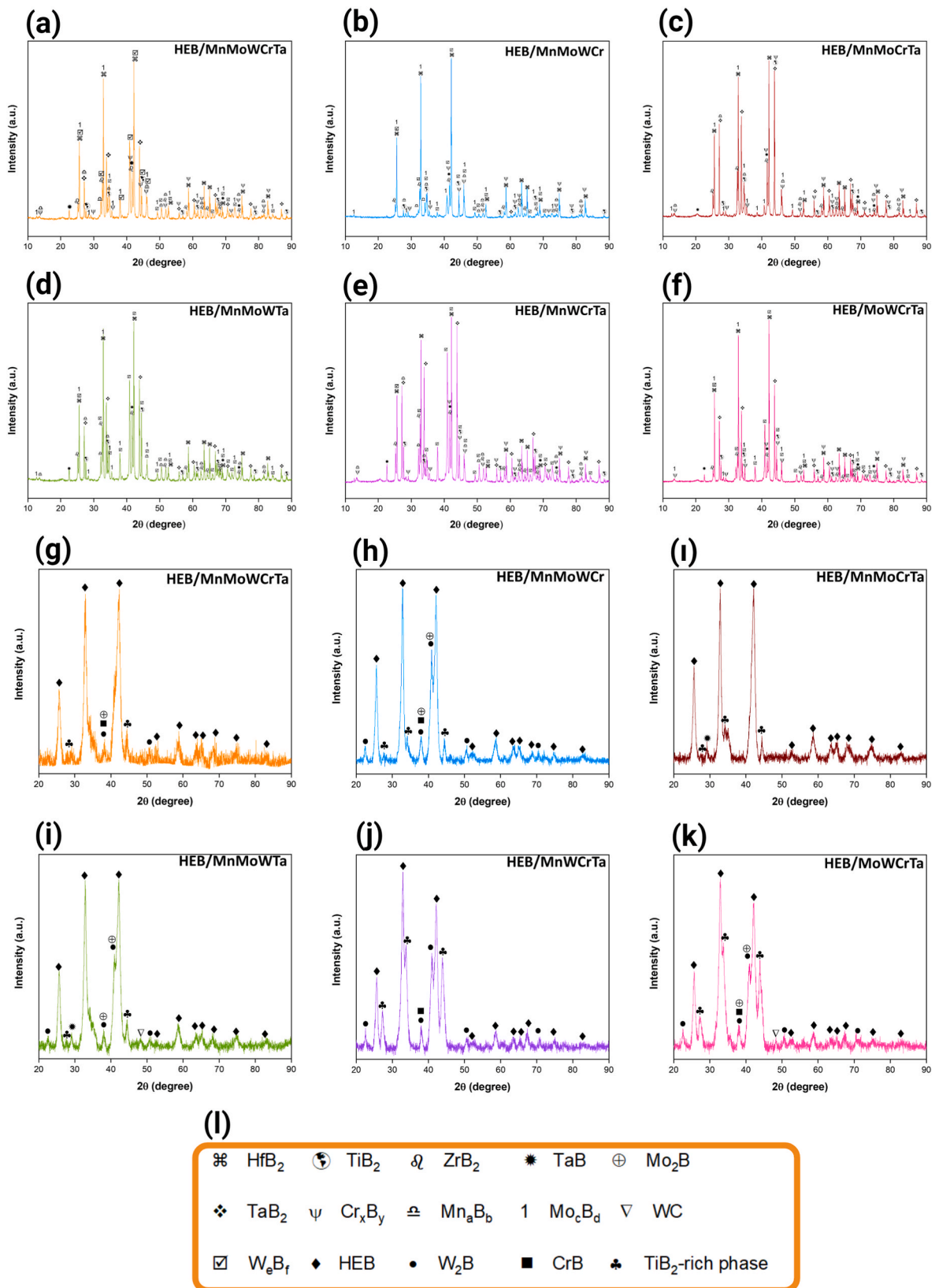

Fig. 1. Schematic diagram of the experimental procedure (Created with BioRender.com).

Fig. 2. (a–l) XRD patterns of the as-blended compositions: (a) HEB/MnMoWCrTa, (b) HEB/MnMoWCr, (c) HEB/MnMoCrTa, (d) HEB/MnMoWTa, (e) HEB/MnWCrTa, (f) HEB/MoWCrTa; (g–k) XRD patterns of the after the HEBM process: (g) HEB/MnMoWCrTa, (h) HEB/MnMoWCr, (ı) HEB/MnMoCrTa, (i) HEB/MnMoWTa, (j) HEB/MnWCrTa, (k) HEB/MoWCrTa, and (l) symbol map.

HEB/MnMoWCrTa has an average value among the seven components. Therefore, there is no relationship between the number of components and powder density. On the other hand, powder density values for seven/eight components increased according to containing three, four, or five powder HEBs [16]. Additionally, differences in high- or low-density components appear to affect the density of values. As an example, the addition of W-boride caused an increase in density. Therefore, it is normal for the composition without W-boride to exhibit the lowest density. Although TaB and Mo-boride additions also significantly affect the change in values, W-boride provides the highest change. As expected, compositions that do not contain Mn boride or Cr boride exhibit higher powder densities [16].

3.2. Characterization of the SPS'd samples

XRD patterns of the SPS'd samples are shown in Fig. 3a–f. All compositions have high-intensity HEB peaks: multi-stoichiometric boride phases or TiB_2-rich regions formed after MA diffused and formed a single-peak HEB structure. HEB phases are defined based on studies in the literature [17,22,29,31,38,41,46]. However, low-intensity HfO_2 (ICDD No: 00-006-0318) or ZrO_2 (ICDD No: 01-078-1807) was formed. A secondary phase is also present in all compositions except HEB/MnMoWCr. There is no matching of the resulting secondary phases with ICDD cards, so they cannot be identified. However, previous studies [17, 22,41,42] observed that compositions containing W or Mo boride formed a secondary phase even in four or five-component compositions. Gild et al. [22] synthesized $(Hf_{0.2}Zr_{0.2}W_{0.2}Mo_{0.2}Ti_{0.2})B_2$ after HEBM and SPS, and they found $(Ti_{1.6}W_{2.4})B_4$ secondary phases. They associated this phase formation with unstable WB_2 or overly stable $(Ti_{1.6}W_{2.4})B_4$. In another study by Gild et al. [42], the synthesis of the $(Hf_{0.2}Zr_{0.2}W_{0.2}Mo_{0.2}Ti_{0.2})B_2$ composition was completed with the borocarbothermal reduction and SPS. They determined by EDS that the secondary phases formed were rich in Mo, W, and Ti. Qin et al. [41] synthesized six different HEB ceramics [$(Ti_{0.2}Zr_{0.2}Hf_{0.2}Mo_{0.2}W_{0.2})B_2$, $(Ti_{0.2}Ta_{0.2}Cr_{0.2}Mo_{0.2}W_{0.2})B_2$, $(Zr_{0.2}Hf_{0.2}Nb_{0.2}Ta_{0.2}W_{0.2})B_2$ $(Zr_{0.225}$ $Hf_{0.225}Ta_{0.225}Mo_{0.225}W_{0.225})B_2$ etc.], with reactive SPS and conventional SPS. As a result of HEBM and conventional SPS, they obtained the HEB and secondary phase; moreover, they confirmed by EDS that these small amounts of phases were W-rich. The formation of secondary phases was due to using non-stoichiometric tungsten boride in that study. Kavak et al. [17] synthesized $(HfTiWZr)B_2$ ceramic with MA and SPS. They detected the primary HEB structure and small amounts of oxide and secondary phases. They said the secondary phases belong to a solid solution or intermetallic compound between (W-Ti)B. Guo et al. [31] produced seven [$(Ti_{1/7}Cr_{1/7}Zr_{1/7}Hf_{1/7}Ta_{1/7}Mo_{1/7}Nb_{1/7})B_2$] and eight component [$(Ti_{1/8}Cr_{1/8}Zr_{1/8}Hf_{1/8}Ta_{1/8}Mo_{1/8}Nb_{1/8}V_{1/8})B_2$] HEB ceramics by ultra-fast high temperature (UHS) method without secondary phase. It is thought that a single-phase HEB structure can be obtained because it does not contain W boride phases; rapid sintering and high temperatures can be reached. When the studies are examined, the secondary phases are thought to be rich in W and Ti. Those formed in the HEB/MnMoCrTa composition may be Mo-rich secondary phases. Additionally, W, Mo, Cr, and Ta have high negative enthalpies of formation, respectively; therefore, may cause solid solutions with different formation enthalpies [41]. Lack or excess of one of these elements triggers the formation of secondary peaks. In addition, CrB_2, despite having low solid solubility, formed a HEB structure as in other publications [22,46]. Moreover, W_2B and TaB used instead of diboride at room temperature can cause the formation of secondary phases [22]. It can be said that many studies have been conducted in which multi-phase HEB synthesis (HEB, oxide, and secondary phases) was mainly performed in production after MA-assisted SPS, and a single-phase structure
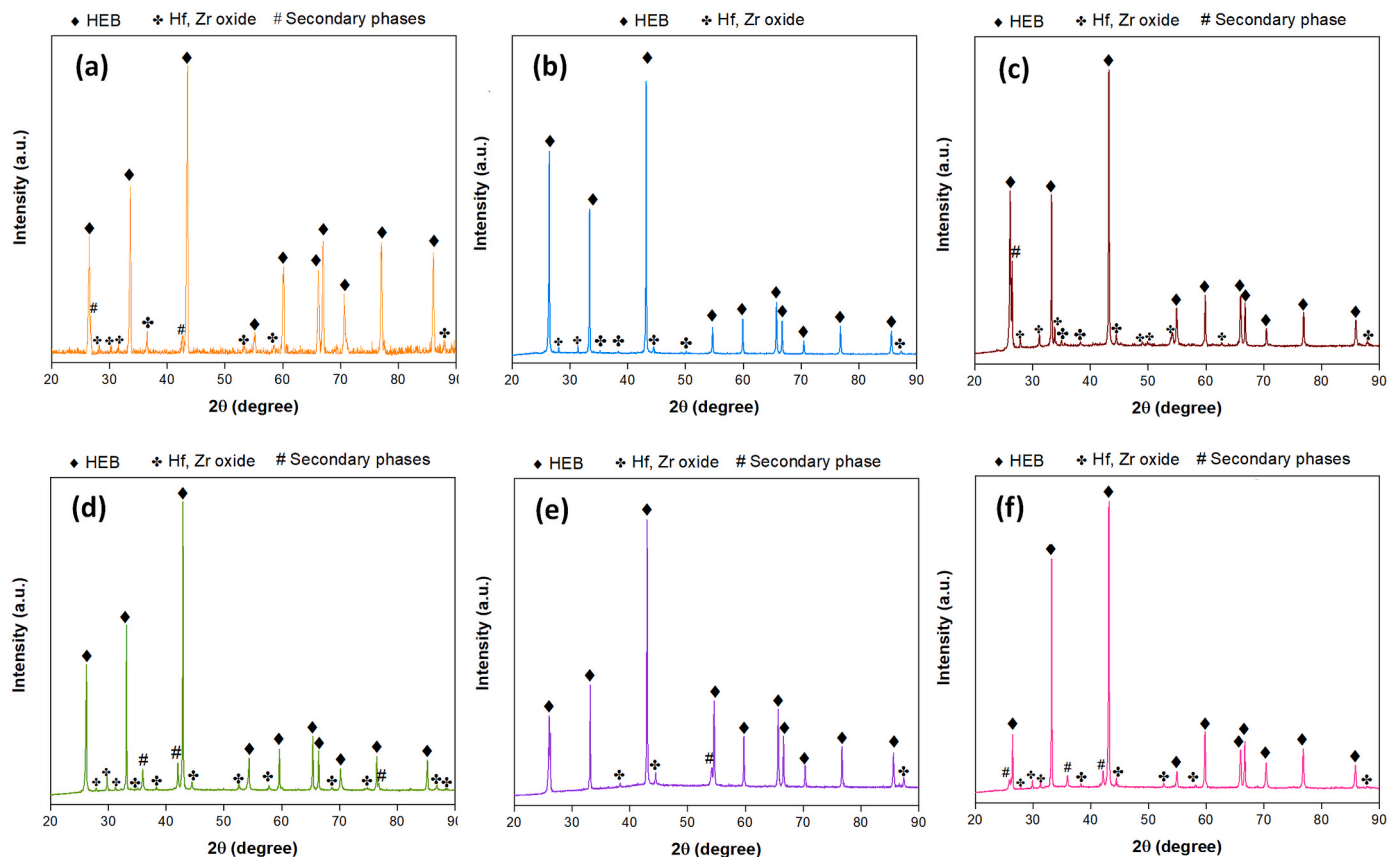

Fig. 3. XRD patterns of the SPS'd samples: (a) HEB/MnMoWCrTa, (b) HEB/MnMoWCr, (c) HEB/MnMoCrTa, (d) HEB/MnMoWTa, (e) HEB/MnWCrTa, (f) HEB/MoWCrTa.

could not be obtained [16,17,22,39,41]. Moreover, adding extra boron may be sufficient to remove oxide phases. However, this may also disrupt the diboride stoichiometry [58]. In contrast, it is more likely to homogenous structure after BCTR and SPS [42]. In addition, most of these studies focused on the production of more than one composition, not a single composition, and evaluations were made between these compositions.

The average Archimedes' densities of the sintered samples are given in Table 2. According to powder density values (Table S3), an increase is observed in all compositions after SPS. However, like the powder density values (Table S3), the lowest Archimedes value is in HEB/MnMoCrTa, but the highest is in HEB/MnMoWTa. Only Archimedes' values were measured; theoretical or relative density values were not calculated like in the previous study [16]. The XRD patterns (Figs. 1 and 2) show that the synthesized boride phases are mostly multi-stoichiometric. In addition, some boride peaks overlap in the XRD patterns. In this case, it is not suitable to calculate the theoretical density using the rule of mixture. Gild et al. [42] did not calculate the theoretical density using similar explanations for Mo-boride. Almost all seven- and eight-component HEBs have higher values than three-, four- or five-component compositions [16]. Kavak et al. [17] also measured the density values of HEBs synthesized at different temperatures, milling times between 7.131 g/cm^3 and 8.054 g/cm^3. Yang et al. [59] measured Archimedes' $(Hf_{0.2}Zr_{0.2}Ta_{0.2}V_{0.2}Nb_{0.2})B_2$ composition, which they synthesized at different temperatures and methods, between 6.86 g/cm^3 and 7.36 g/cm^3. Gild et al. [22] reached experimental densities of 7.87 g/cm^3 and 7.36 g/cm^3 for $(Hf_{0.2}Zr_{0.2}Ta_{0.2}Mo_{0.2}Ti_{0.2})B_2$ and $(Hf_{0.2}Zr_{0.2}Ta_{0.2}Cr_{0.2}Ti_{0.2})B_2$, respectively. Here, this density value increased with the addition of MnB_2 and W_2B to the $(Hf_{0.2}Zr_{0.2}Ta_{0.2}Mo_{0.2}Ti_{0.2})B_2$ composition (HEB/MnMoWTa). However, lower densities were exhibited in other cases. In addition, higher Archimedes' values were found in the cases of MoB_2 and W_2B added to the $(Hf_{0.2}Zr_{0.2}Ta_{0.2}Mo_{0.2}Ti_{0.2})B_2$ composition (HEB/MoWCrTa). The measured values contain similar or higher results than the literature. It should be noted that the existence of secondary phases or the amount of porosity also affects the density.

The additional elements significantly affect high-entropy boride ceramics' microstructure, compositions, and overall properties. The system's entropy is increased when more elements are added, which may allow the system to stabilize single-phase solid solutions even at high temperatures. Furthermore, introducing additional elements may lead to the formation of secondary phases, which depend on matrix interactions. For instance, the Hf, Ta, and Zr contribute to increased hardness and strength because these elements generate strong covalent bonds with boron. When Hf, Ta, and Nb are combined, the thermal stability is increased while phase stability is maintained. The addition of Ti, Nb, and Cr significantly improved the oxidation resistance, with these elements forming protective oxide layers. Also, the Zr and Nb combination increased the toughness and ductility [60,61]. Ti contributes to forming solid solutions, enhancing the ceramic's stability with phases such as $(Ti, Nb, Ta)B_2$. Formation of $(Zr, Hf)B_2$ phases also contributes to the structural integrity due to the influence of their larger atomic radii. According to particular contributions, such phases like $(Ti, Zr, Hf, Nb, Mo)B_2$ form ceramics with very high hardness and thermal stability [62]. Adding Ta and Mo to the Hf-Zr-Ti base generates higher

yield hardness [63]. Moreover, W and Mo additions to Hf-Zr-Ti lead to distortion at Hf-lattice to provide an increment in hardness [64]. In the presented study, the effect of the elemental combination of (Hf, Ti, Zr, Mn, Mo) with the addition of W + Ta, Cr + Ta, and W + Cr. The combined effect of W, Cr, and Ta was also examined. The presence of Ta, in particular combination with W, significantly increased the density. The W, Cr, and Ta combination also showed a substantial impact, although slightly less than the W + Ta combination. According to the density results of Mn, Mo, and Mn + Mo addition to (Hf, Ti, Zr, W, Cr, Ta) basis, Mn and Mo together resulted in a higher density when each element was added individually. Thus, Mn + Mo + Ta resulted in the highest density rather than the Mn + Mo + Ta + Cr + W combination.

SEM and color EDS images at different magnifications of the SPS'd samples are given in Fig. 4a–b. Additionally, EDS analysis results are shown for each composition in Fig. 4c. Also, the numerical values of the EDS are given in Table S.4-Table S.9. According to Fig. 4a–b, different phases are formed in the structure. The resulting phases are distributed in inhomogeneous and irregular shapes on the matrix. Additionally, porosity is observed in all compositions. Also, different studies found porosity in HEB compositions [65,66]. Grain boundaries are clearly evident. Eutectic regions have formed in the composition of HEB/MnMoWCrTa. Like the previous study, the eutectic composition is thought to occur between Mn and Cr because of their low melting point [16]. Similarly, dominant melt regions are present in HEB/MnMoCrTa and HEB/MnMoWCr. On the contrary, at the HEB/MnMoWTa composition, these regions decrease, and instead, the non-homogeneous distribution of light-colored dots is observed. The contrast difference is more pronounced in the HEB/MnWCrTa. According to EDS results in HEB/MnMoWCrTa composition, elemental distributions are close to each other, although not homogeneous. Mn is less than 10 % atomic. Although Hf is dominant at point 1, all points have a close distribution. Similarly, Mn in HEB/MnMoWCr is below 10 % except for a single point. Regarding the third point, Hf and Zr dominant regions are formed. HEB/MnMoCrTa composition is also similar to Mn. The remaining components are distributed in a relatively close to one another cluster. In the composition that does not contain Cr boride, Mn increased atomically. In HEB/MnWCrTa, boron was found at one point. A similar microstructure occurs in the HEB/MoWCrTa composition. As a result of Mn deficiency, no melt zones were formed. Mo is in low amounts, while Hf is atomically dominant. Elements with low atomic weight are difficult to detect in EDS. However, the presence of overlapping peaks also affects the EDS results. It should also be noted that EDS is a semi-quantitative method. Different diffusion rates, elemental differences, dissolution rates of borides within each other, porosities, grain size, and solid solution formation explain the change in microstructures [16,17,67]. In our previous study [16], $(HfTiZrMnCr)B_2$ was synthesized as a five-component HEB ceramic using the same method. The particles were scattered together with the melted regions, forming an almost stony appearance. This study, shows similar SEM images are seen in HEB/MnMoWCrTa, HEB/MnMoWCr, HEB/MnMoCrTa, and HEB/MnMoWTa. Although it is thought that Mn and Cr have this effect, Mo, which is common in all compositions, may also cause similar shapes. In addition, HEB/MnWCrTa and HEB/MoWCrTa have similar SEM images among themselves. Here, WCrTa had a better effect when combined. Mn and Cr are more prone to forming melted points because their melting points are low. This situation is partially correct in the HEB/MnMoWCrTa system due to the high entropy effect. In the study conducted by Gild et al. [22], different HEB ceramics such as $(Hf_{0.2}Zr_{0.2}W_{0.2}Mo_{0.2}Ti_{0.2})B_2$ and $(Hf_{0.2}Zr_{0.2}Ta_{0.2}Mo_{0.2}Ti_{0.2})B_2$ were synthesized. Although more homogeneous images were observed in both compositions, discrete structures were formed in low amounts. In this study, similarly, more homogeneous and low amounts of discrete images were formed in the addition of CrTa (HEB/MoWCrTa) to WMo. However, more discrete and scattered particles were observed in the addition of MnTa (HEB/MnMoWTa) to WMo. Therefore, it can be predicted that Mn disrupts the homogeneity to a greater extent than Cr.

Table 2
Average Archimedes' densities of the sintered samples.

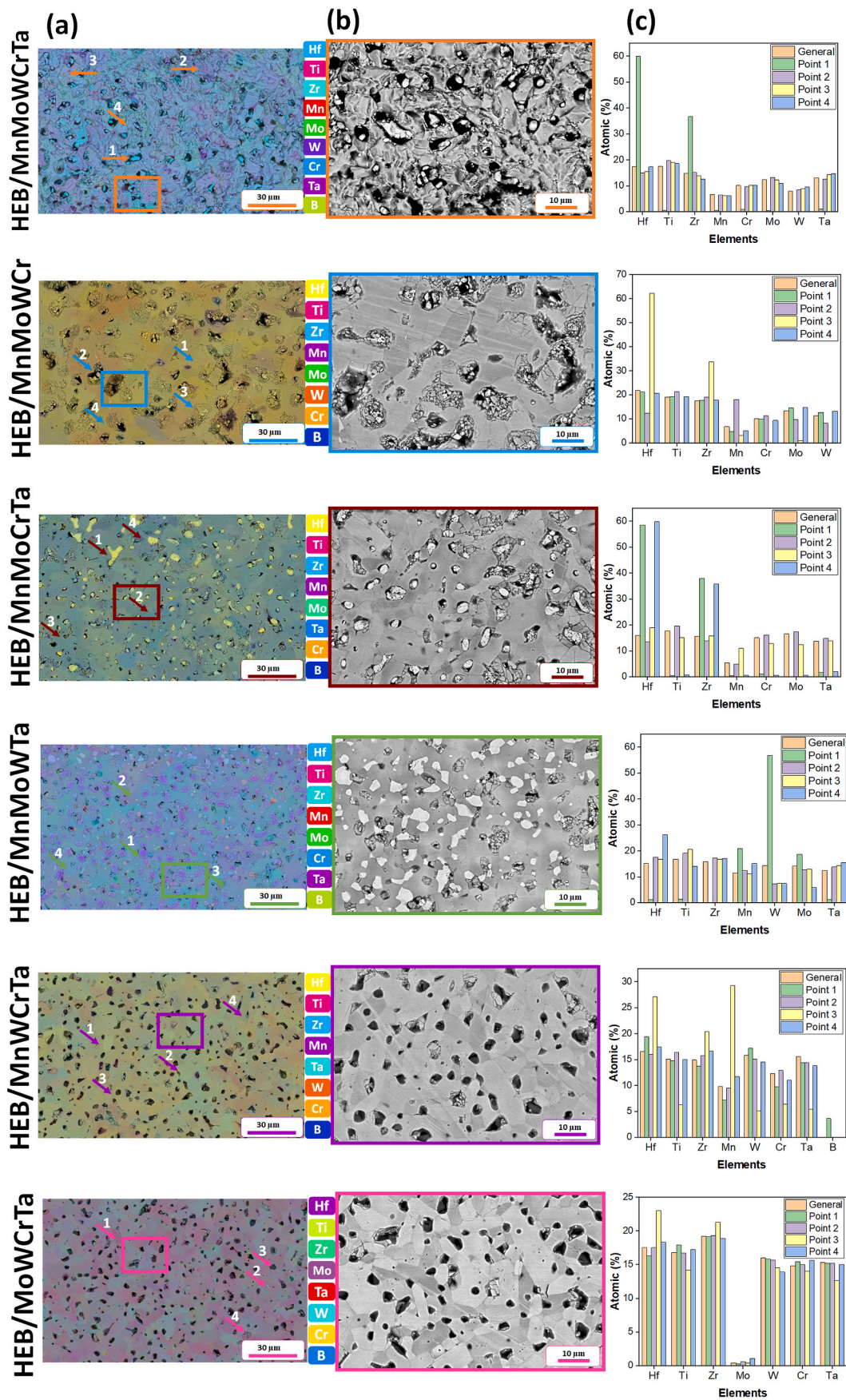| Sample	Average Archimedes' Density (g/cm^3)
HEB/MnMoWCrTa	7.4794 ± 0.0065
HEB/MnMoWCr	7.0766 ± 0.0019
HEB/MnMoCrTa	6.9134 ± 0.0032
HEB/MnMoWTa	7.9495 ± 0.0053
HEB/MnWCrTa	7.3325 ± 0.0067
HEB/MoWCrTa	7.4477 ± 0.0018

Fig. 4. SEM images of the SPS'd samples at different magnifications: (a) color SEM images, (b) SEM images, and (c) EDS analysis results. (For interpretation of the references to color in this figure legend, the reader is referred to the Web version of this article.)

A popular open-source program for processing and analyzing images, ImageJ was created by the National Institutes of Health (NIH) [68]. It allows using a variety of image processing tools such as filtering, thresholding, segmentation, and a bunch of measurements. The processing methods are based on gray values of images according to pixels [69,70]. Fig. 5a shows the original SEM image for HEB/MnMoWCrTa (representative of a step-by-step guide), and Fig. 5b is the measurement line of which results are given in Fig. 5c. The plot analysis (Fig. 5c) gave the intensity profile along with line according to brightness of each pixels. Fig. 5d shows the gray values of each pixel, which was pre-measured and graphed in Fig. 5c. Each valley of Fig. 5d represents the whites because of minimum gray values. The distance was rescaled according to the legend of SEM images, which was 10 μm. The 10 μm legend bar was measured with a line tool to correlate pixels of images with a known distance. According to % gray containment, the segmentation was applied with the threshold tool. The white and black region ratios were calculated according to the % gray of each pixel. After detecting the white and black regions, the gray area ratio, which fluctuates in a wide range, was calculated by comparing the ratios determined precisely and 100 %. The image segmentation is based on back mapping, allowing scatter plots to be generated from the 8-bit grayscale images [71,72]. The gray scaling is giving probability of pixels appearance [73,74]. Also, noise, which refers to random variations in brightness, reduction of images was applied with the deconvolution method [75]. These details guided the processing of the SEM images used in the study, which reduced noise to a level appropriate for phase identification. The phase ratio determination process was started immediately without the need for extra color modifications because the photos were already in grayscale. The phase ratio was measured using the threshold method and the gray values as a guide. Using this procedure, the values of that tool were used to determine the ratios of regions devoid of gray. Relevant literature studies provide additional support for the stability of the employed approach.

ImageJ software estimated HEB phase amount, porosity, and secondary/oxide phases from SEM images. The images from the software showing the phase distributions are given in Fig. 6, and the numerical values are given in Table S.10. The lowest amount of HEB is in the eight-component system (~77 %), and the highest is in HEB/MnMoCrTa (~89 %). The amount of HEB phase in all compositions is over 70 %. Besides, the HEB compositions are above 82 %, except for HEB/MoWMnCr and the eight-component system. Moreover, the composition with the lowest porosity amount is HEB/MnMoWTa (~3 %), and the highest is HEB/MnMoWCr (~13 %). In addition, except for HEB/MnMoWCrTa, porosity amounts are below 10 %. However, the compositions with the highest percentage of oxide and/or secondary phases are HEB/MnMoWTa (13.58 %) and HEB/MoWCrTa (13.42 %), which contain the most minor porosity. Also, except for HEB/MnMoWCrTa, the secondary/oxide phases are well below 10 %. In HEB/MnMoWCrTa, both porosity and the number of oxide and/or secondary phases are high. However, the situations in which Mo boride and W boride are present together but not Mn boride and Cr boride are pretty similar (HEB/MnMoWTa and HEB/MoWCrTa). Our previous study [16] stated that high amounts of HEB containing Mn boride and Cr boride could be achieved. It is understood that when the number of elements increases, the change becomes different, and the disorder increases. In the eight-component system, a decrease in the amount of HEB can be expected due to the high-entropy effect. Apart from this, the amount of TaB directly affected the HEB ratio in seven components.

Hardness values-HEB amount and hardness values-secondary phases graphs for the SPS'd samples are given in Fig. 7a–b, respectively. In addition, the hardness values are in Fig. 7c. HEB/MnMoWCr and HEB/MnMoWCrTa have the highest and lowest values, respectively. Although there are slight differences between the compositions, the hardness values are close to each other on average. Moreover, it can be seen that hardness in seven systems is around 23 GPa and above. In addition, increasing the number of components showed that the results decreased significantly. Guo et al. [31] found the hardness values measured under HV_1 in HEBs with seven and eight components synthesized by UHS to be approximately 21 and 18.5 GPa, respectively. Again, as stated in that study [31], slip systems may become complex in systems with more elements, and as a result, mechanical properties are negatively affected. In addition, in seven-component compositions, the values are very close. Moreover, in his study, Yeh [51] calculated the configurational entropy of up to thirteen elements in equimolar alloys. It was calculated that the
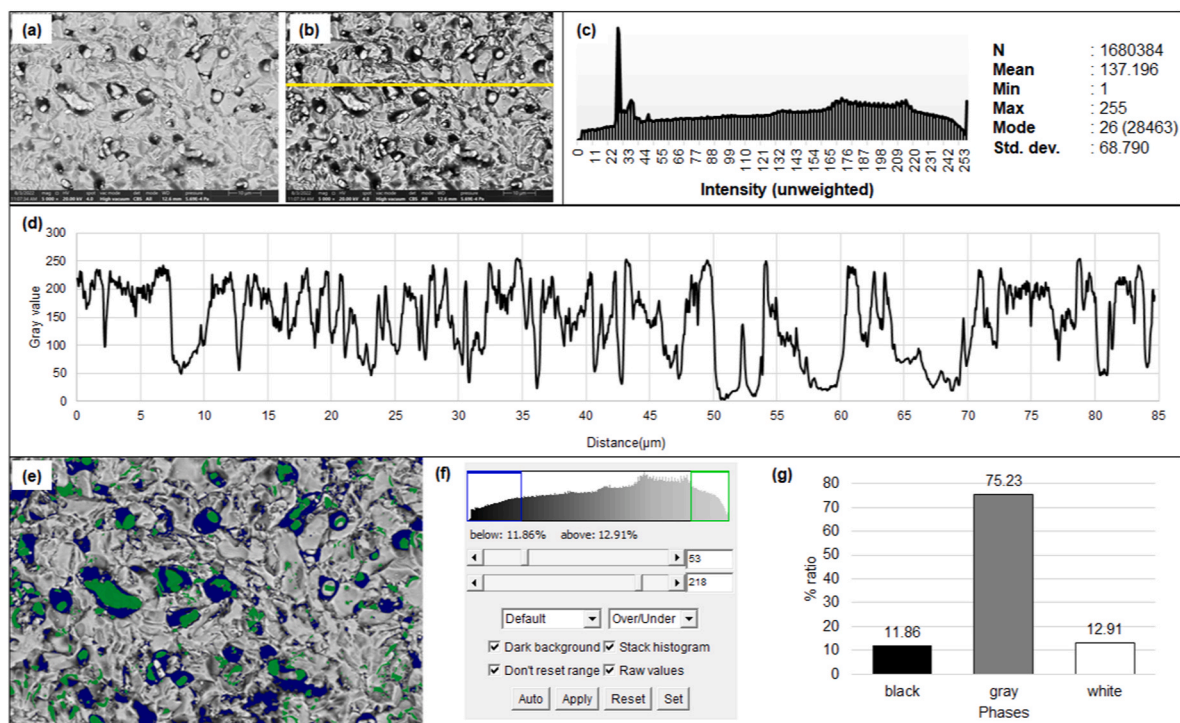

Fig. 5. (a–g) Image processing for phase ratio measurement (step-by-step), representative for the HEB/MnMoWCrTa sample.
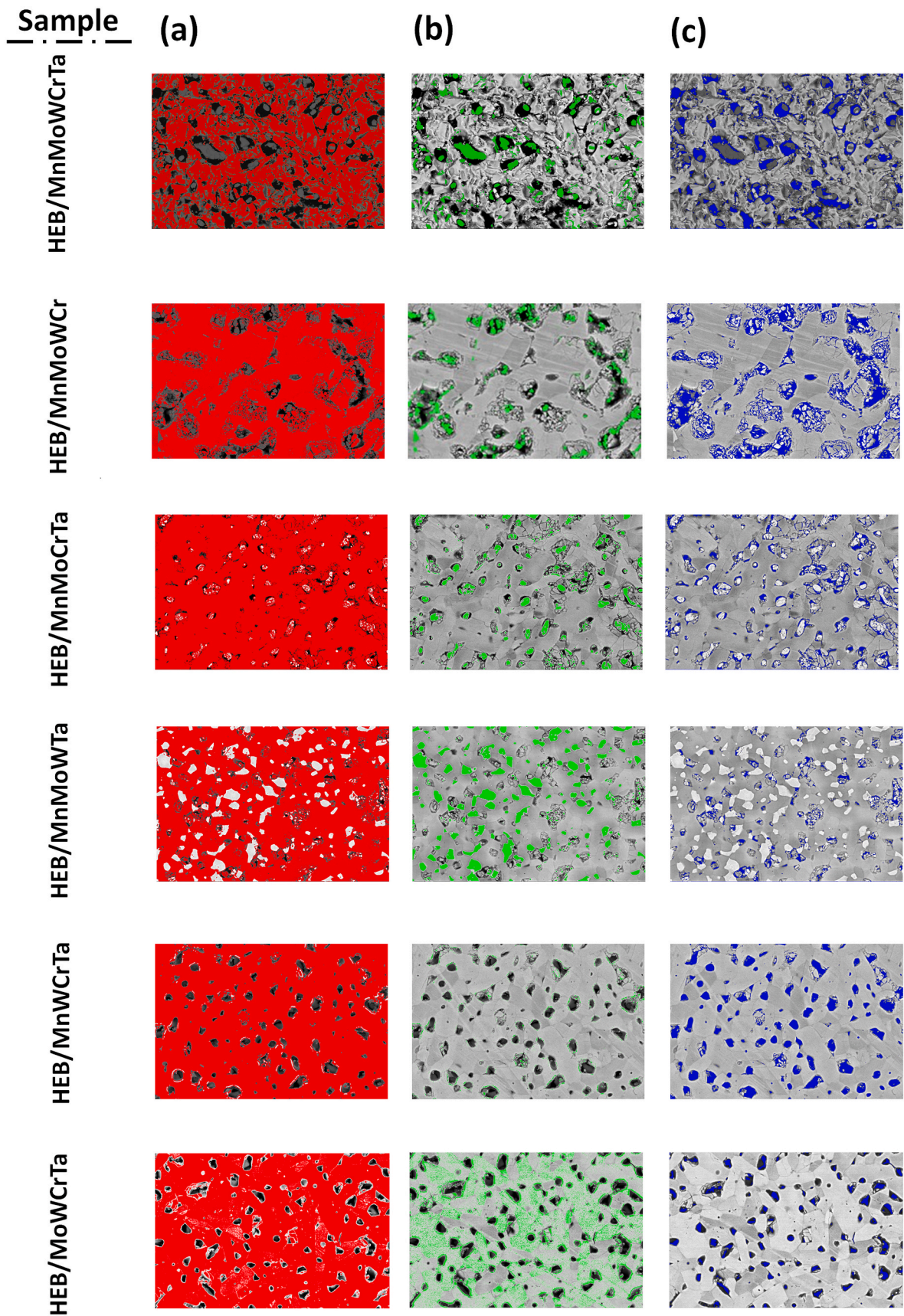
Fig. 6. Phase distribution of the SPS'd sample taken from ImageJ software: (a) HEB phase, (b) secondary phase/oxides, and (c) porosity.
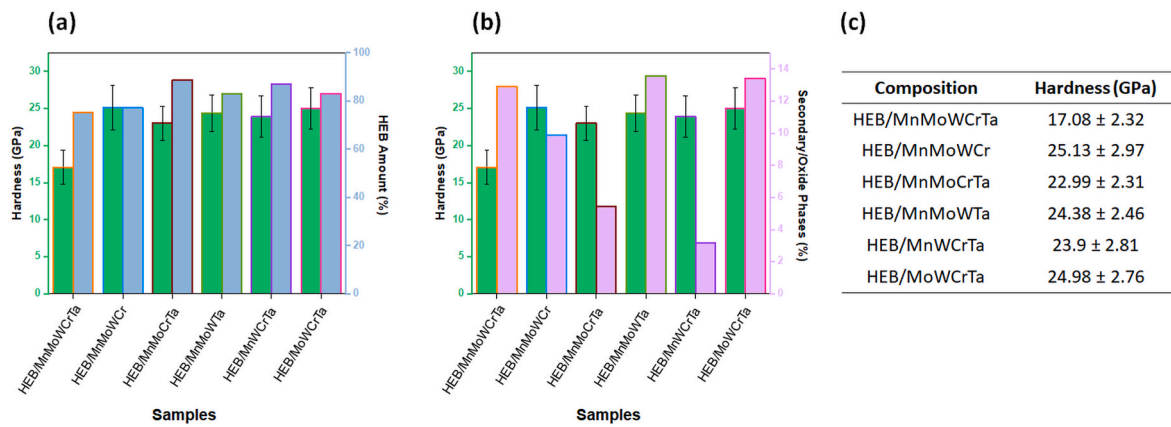
Fig. 7. (a) Hardness values (green) and HEB amount (blue), (b) Hardness values (green) and secondary phases (purple) graphs, (c) hardness results for the SPS'd samples. (For interpretation of the references to color in this figure legend, the reader is referred to the Web version of this article.)

configurational entropy exceeded one after three elements and reached 1.61R after five elements. However, after adding eleven elements, the increase slowed and became linear. It is thus understood that as the number of elements increases, significant progress cannot be achieved due to the high entropy effect [51]. Here, HEB/MnMoCrTa and HEB/MnWCrTa show the lowest values. Zhou et al. [76] calculated the hardness values of diborides with the density functional theory (DFT) method and listed the hardness values from highest to lowest: TiB_2, ZrB_2, HfB_2, TaB_2, CrB_2, MoB_2, WB_2, MnB_2. However, compositions that do not contain W boride and Mo boride are expected to have higher hardness. Surprisingly, in different studies, hardness values in HEB compositions containing Mo boride and/or W boride were higher than those of other synthesized components [22,31,41]. On the other hand, HEB/MnMoWCr without TaB_2 has the highest hardness. TaB was used as the starting powder in this study, and elemental boron was added to ensure stoichiometry. This situation may also affect hardness. Additionally, as expected, compositions that do not contain Mn boride and Cr boride also have high values. In secondary phases, the presence of borides that cannot be synthesized stoichiometrically, compounds, and the amount of porosity and HEB phases also affect hardness [16,17,24,32,41]. HEB amount and secondary phases calculated with ImageJ were also compared with the hardness results. As expected, the hardness reached its lowest value at the HEB/MnMoWCrTa value, where the amount of HEB was the lowest. Apart from this, the compositions of HEB/MoWCrTa and HEB/MnMoWTa are similar regarding both hardness and the amount of HEB and secondary phase. Additionally, if the secondary phase formed is more complex it may also increase the hardness of HEB compounds [42]. The hardness values and HEB amounts are very close in all compositions. Elemental differences affect the distribution in seven-component compositions. The solubility of different elements in each other is also different. As a result, mechanical properties can be directly or indirectly affected [41]. HEB/MnMoWCr and HEB/MoWCrTa have the two highest hardness values. When the compositions are examined, it can be said that MnB_2 positively affects the hardness value compared to TaB. Binary boride compounds, which are theoretically thought to have the lowest values, are included in this composition. Surprisingly, as mentioned above, these compositions require higher hardness values. HEB/MnMoWTa and HEB/MoWCrTa exhibit similar numbers. Here, CrB_2 increased the hardness value compared to MnB_2. Again, HEB/MnMoCrTa and HEB/MnWCrTa provide close values compared to each other. Here, W_2B exhibited superior values compared to MoB_2. In the compositions that exhibit the lowest (HEB/MnMoCrTa) and highest (HEB/MnMoWCr) values among the seven compositions, W_2B exhibited much higher values. In our previous study [16], $(HfTiZrMnCr)B_2$ composition had a hardness value of approximately 27 GPa. However, these values could not be reached here. Gild et al. [22] reached hardness values of approximately 19 and 18 GPa in

$(Hf_{0.2}Zr_{0.2}Ta_{0.2}Mo_{0.2}Ti_{0.2})B_2$ and $(Hf_{0.2}Zr_{0.2}Ta_{0.2}Cr_{0.2}Ti_{0.2})B_2$ compositions produced with MA and SPS (200 kgf/mm^2, 15 s), respectively. Here, they emphasized that the hardness values depend on porosity and microstructure. Again, in another study by Gild et al. [42], they calculated approximately 25 GPa in $(Hf_{0.2}Zr_{0.2}Ta_{0.2}Cr_{0.2}Ti_{0.2})B_2$ composition produced with BCTR and SPS, and measured the hardness value under the same conditions. $(Hf_{0.2}Zr_{0.2}Ta_{0.2}Cr_{0.2}Ti_{0.2})B_2$ produced by Zhang et al. [46] with BCTR and textured SPS has a value of approximately 30 GPa. Values such as production method and production parameters also significantly affect the results.

Wear rate, wear rate results, and corresponding 2-D profile graphs of the SPS'd samples are shown in Fig. 8a–h. Additionally, optical microscope images of wear marks are shown. HEB/MnMoWCrTa has the lowest and HEB/MnMoCrTa has the highest wear resistance. The wear rate values of HEB/MnMoWCr and HEB/MnMoCrTa compositions are almost the same. Hardness and wear resistance almost confirm each other. Additionally, when the images and profile graphics of the wear marks are examined together, it is understood that the abrasive wear mechanism is dominant in HEB ceramics. Delamination is especially evident in the optical microscope wear trace of the HEB/MnMoWCrTa composition. Along with elemental differences, secondary phases, grain size, pore size, and porosities also affect wear resistance [16,17]. So far, a few studies have examined the wear resistance of HEB ceramics. However, Kavak et al. [17] tested the $(HfTiWZr)B_2$ composition, which they synthesized at different temperatures under conditions similar to those in this article. The wear resistance decreased as the amount of porosity increased. Our previous study [16] observed that secondary phases, porosity, and elemental differences affect wear resistance. Besides, in the same study, the wear rates of $(HfTiZrMnCr)B_2$ and $(HfTiMnCr)B_2$ were approximately 2×10^{-6} and 6×10^{-6}, respectively. The hardness values show that wear resistance has improved in seven-component systems compared to the eight-component composition. However, it needs to be corrected to interpret seven-component systems as increasing or decreasing compared to each other. Here too, MnMoCrTa exhibits the highest strength. Also, compositions containing MnCr (except HEB/MnMoWCrTa) meet higher wear values. Apart from this, MoTa showed better properties compared to MoW. WTa exhibited lower strength compared to these pairs. In addition, Ta made a positive contribution to wear resistance compared to W (HEB/MnMoWCr, HEB/MnMoCrTa). However, when a comparison is made between Mo and Ta (HEB/MnMoWCr and HEB/MnWCrTa), Mo has the upper hand over Ta. Similarly, wear values decreased in both compositions containing WTa (HEB/MnMoWTa and HEB/MoWCrTa). In addition, it can be said that Cr made a positive contribution to wear resistance compared to Mn by looking at these two compositions (HEB/MnMoWTa and HEB/MoWCrTa). Additionally, since the compositions are different, it would be more accurate to interpret only the effect of boride compounds
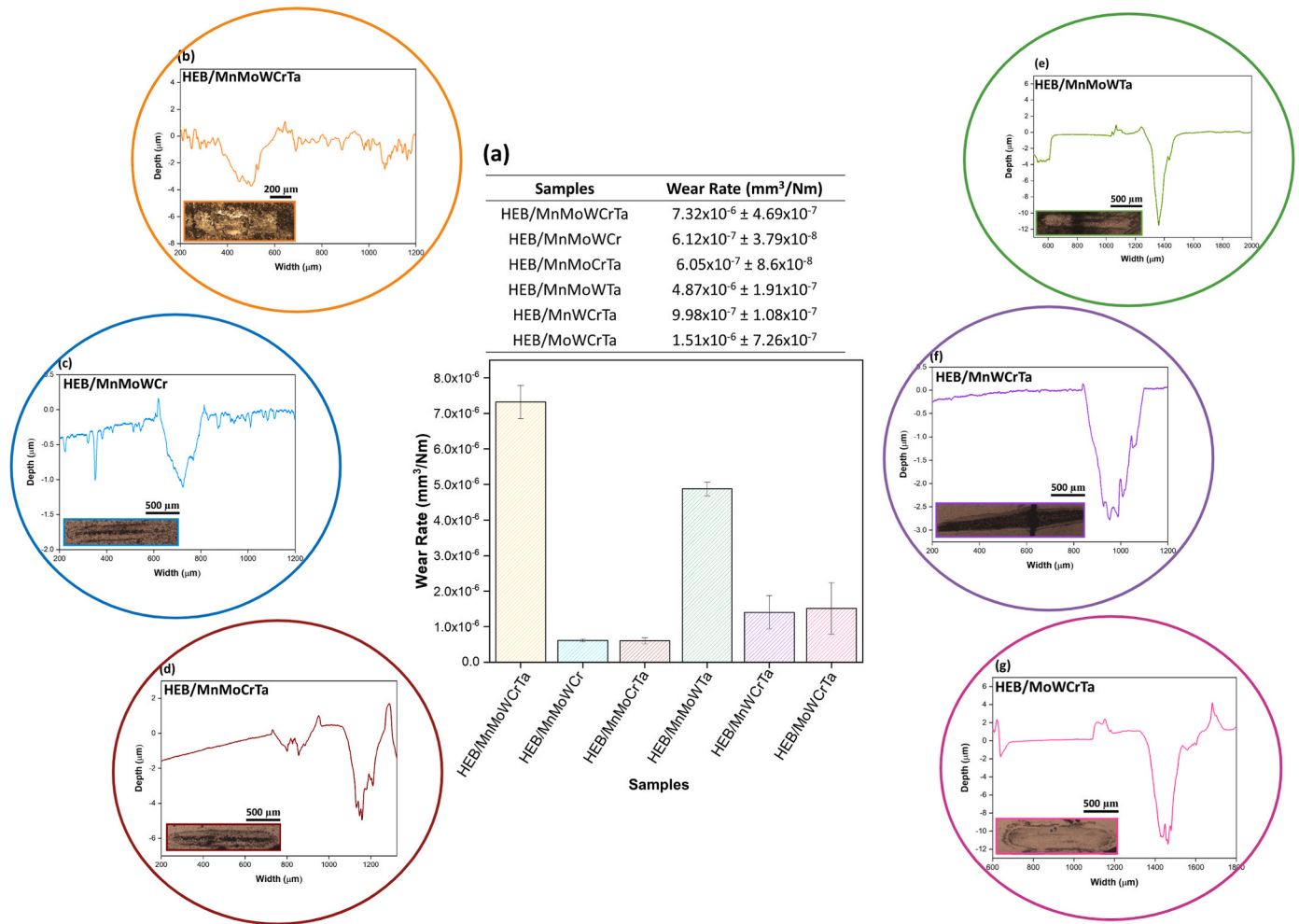
Fig. 8. (a) Wear rate graph and results, and corresponding 2-D profile graphs of the SPS'd samples: (b) HEB/MnMoWCrTa, (c) HEB/MnMoWCr, (d) HEB/MnMoCrTa, (e) HEB/MnMoWTa, (f) HEB/MnWCrTa, (g) HEB/MoWCrTa.

on wear resistance rather than comparing them.

4. Conclusions

This study investigated the possibility of synthesizing seven- and eight-component HEB ceramics by high-energy ball milling (6 h) assisted spark plasma sintering (2000 °C, 30 MPa) and the effect of elemental differences on the composition. Also, detailed phase analysis, and microstructural, physical and mechanical characterization were carried out on the powder and SPS'd samples. The results are summarized below:

- After 6 h of MA, HEB peaks began to form. However, there are several secondary boride and TiB_2-rich phases.
- After SPS, it was observed that the dominant peaks belonged to the HEB phases. However, low amounts of Hf/Zr oxides, and secondary phases were also formed. No secondary peak formation was observed in HEB/MnMoWCr.
- The highest density value of SPS'd samples measured by Archimedes' is observed in the HEB/MnMoWTa (7.9495 ± 0.0053 g/cm^3) composition, and the lowest density value is in the HEB/MnMoCrTa (6.9134 ± 0.0032 g/cm^3).
- The HEB/MoWCrTa and HEB/MnMoWCrTa have the highest (24.98 GPa) and lowest (17.08 GPa) hardness values, respectively. The hardness values of the seven-component compositions are very close to each other (average 24.2 GPa).

- The wear rates of the samples are very close. On the other hand, HEB/MnMoWCrTa (7.32×10^{-6} mm^3/Nm) has the lowest and the highest one belongs to HEB/MnMoCrTa (6.05×10^{-6} mm^3/Nm).

According to all results, seven- and eight-component compositions can be successfully synthesized with MA and SPS. In addition, different boride components change the mechanical properties.

CRediT authorship contribution statement

İlayda Süzer: Writing – original draft, Investigation, Formal analysis. **Amir Akbari:** Investigation. **Semih Ates:** Writing – original draft, Investigation. **Kübra Gürcan Bayrak:** Writing – original draft, Investigation. **Sıddıka Mertdinç-Ülküseven:** Writing – original draft, Investigation. **C. Fahir Arisoy:** Writing – review & editing. **M. Lütfi Öveçoğlu:** Writing – review & editing. **Duygu Ağaoğulları:** Writing – original draft, Supervision, Project administration, Conceptualization.

Declaration of competing interest

The authors declare that they have no known competing financial interests or personal relationships that could have appeared to influence the work reported in this paper.

Data availability

Data will be made available on request.

Acknowledgment

Appendix A. Supplementary data

Supplementary data to this article can be found online at https://doi.org/10.1016/j.rineng.2024.102976.

References

[1] T. Ayode Otitoju, P. Ugochukwu Okoye, G. Chen, Y. Li, M. Onyeka Okoye, S. Li, Advanced ceramic components: materials, fabrication, and applications, J. Ind. Eng. Chem. 85 (2020) 34–65, https://doi.org/10.1016/j.jiec.2020.02.002.

[2] D. Ağaoğullari, I. Duman, M.L. Öveçoğlu, Synthesis of LaB 6 powders from La 2O 3, B 2O 3 and Mg blends via a mechanochemical route, Ceram. Int. 38 (2012) 6203–6214, https://doi.org/10.1016/j.ceramint.2012.04.073.

[3] C. Qi, Y. Jiang, Y. Liu, R. Zhou, Elastic and electronic properties of XB2 (X=V, Nb, Ta, Cr, Mo, and W) with AlB2 structure from first principles calculations, Ceram. Int. 40 (2014) 5843–5851, https://doi.org/10.1016/j.ceramint.2013.11.026.

[4] D. Ağaoğullari, Ö. Balcı, N. Akçamlı, İ. Duman, M.L. Öveçoğlu, Effects of different milling conditions on the properties of lanthanum hexaboride nanoparticles and their sintered bodies, Ceram. Int. 45 (2019) 18236–18246, https://doi.org/10.1016/j.ceramint.2019.06.034.

[5] A. Paksoy, M. Buldu-Akturk, S. Arabi, E. Erdem, Ö. Balcı-Çağıran, Synthesis and capacitive performance of ZrB2 and its composites as supercapacitor electrodes, Solid State Sci 142 (2023) 107256, https://doi.org/10.1016/j.solidstatesciences.2023.107256.

[6] S. Mertdinç-Ülküseven, F. Khakzad, C. Aslan, K. Onbasli, Ç. Çevik, S. İşçi, Ö. Balcı-Çağıran, H. Yagci Acar, M.L. Öveçoğlu, D. Ağaoğulları, Fe2B magnetic nanoparticles: synthesis, optimization and cytotoxicity for potential biomedical applications, J. Sci. Adv. Mater. Devices. 8 (2023) 100602, https://doi.org/10.1016/j.jsamd.2023.100602.

[7] J.W. Yeh, S.K. Chen, S.J. Lin, J.Y. Gan, T.S. Chin, T.T. Shun, C.H. Tsau, S.Y. Chang, Nanostructured high-entropy alloys with multiple principal elements: novel alloy design concepts and outcomes, Adv. Eng. Mater. 6 (2004) 299–303, https://doi.org/10.1002/adem.200300567.

[8] B. Cantor, I.T.H. Chang, P. Knight, A.J.B. Vincent, Microstructural development in equiatomic multicomponent alloys, Mater. Sci. Eng. 375–377 (2004) 213–218, https://doi.org/10.1016/j.msea.2003.10.257.

[9] D.B. Miracle, O.N. Senkov, A critical review of high entropy alloys and related concepts, Acta Mater. 122 (2017) 448–511, https://doi.org/10.1016/j.actamat.2016.08.081.

[10] J.W. Yeh, Y.L. Chen, S.J. Lin, S.K. Chen, High-entropy alloys – a new era of exploitation, Mater. Sci. Forum 560 (2007) 1–9, https://doi.org/10.4028/www.scientific.net/msf.560.1.

[11] S. Guo, C. Ng, J. Lu, C.T. Liu, Effect of valence electron concentration on stability of fcc or bcc phase in high entropy alloys, J. Appl. Phys. 109 (2011), https://doi.org/10.1063/1.3587228.

[12] K.Y. Tsai, M.H. Tsai, J.W. Yeh, Sluggish diffusion in Co-Cr-Fe-Mn-Ni high-entropy alloys, Acta Mater. 61 (2013) 4887–4897, https://doi.org/10.1016/j.actamat.2013.04.058.

[13] B. Cantor, Multicomponent high-entropy Cantor alloys, Prog. Mater. Sci. 120 (2021) 100754, https://doi.org/10.1016/j.pmatsci.2020.100754.

[14] Q. Zhou, F. Xu, C. Gao, W. Zhao, L. Shu, X. Shi, M.F. Yuen, D. Zuo, Design of high-performance high-entropy nitride ceramics via machine learning-driven strategy, Ceram. Int. 49 (2023) 25964–25979, https://doi.org/10.1016/j.ceramint.2023.05.147.

[15] C.M. Rost, E. Sachet, T. Borman, A. Moballegh, E.C. Dickey, D. Hou, J.L. Jones, S. Curtarolo, J.P. Maria, Entropy-stabilized oxides, Nat. Commun. 6 (2015), https://doi.org/10.1038/ncomms9485.

[16] İ. Süzer, S. Ates, A. Akbari, S. Mertdinç-Ülküseven, K. Gürcan Bayrak, E. Aysel, E. Ayas, C.F. Arisoy, M.L. Öveçoğlu, D. Ağaoğulları, (HfTiZrMnCr)B2 high entropy diboride ceramics: synthesis mechanism, microstructural, mechanical and thermal characterization, J. Mater. Res. Technol. 27 (2023) 298–315, https://doi.org/10.1016/j.jmrt.2023.09.246.

[17] S. Kavak, K.G. Bayrak, M. Mansoor, M. Kaba, E. Ayas, Ö. Balcı-Çağıran, B. Derin, M.L. Öveçoğlu, D. Ağaoğulları, First principles calculations and synthesis of multi-phase (HfTiWZr)B2 high entropy diboride ceramics: microstructural, mechanical and thermal characterization, J. Eur. Ceram. Soc. 43 (2023) 768–782, https://doi.org/10.1016/j.jeurceramsoc.2022.10.047.

[18] E. Castle, T. Csanádi, S. Grasso, J. Dusza, M. Reece, Processing and properties of high-entropy ultra-high temperature carbides, Sci. Rep. 8 (2018) 1–12, https://doi.org/10.1038/s41598-018-26827-1.

[19] J. Shi, H. Jiang, X. Hong, J. Tang, Non-noble metal high entropy sulfides for efficient oxygen evolution reaction catalysis, Appl. Surf. Sci. 642 (2024) 158598, https://doi.org/10.1016/j.apsusc.2023.158598.

[20] C. Liu, M. Kuang, C. Bao, K. Xiang, F. Shen, H. Liu, The design of high-entropy metal sulfides promising high-performance gaseous elemental mercury removal, Fuel 361 (2024) 130659, https://doi.org/10.1016/j.fuel.2023.130659.

[21] J. Gild, J. Braun, K. Kaufmann, E. Marin, T. Harrington, P. Hopkins, K. Vecchio, J. Luo, A high-entropy silicide: (Mo0.2Nb0.2Ta0.2Ti0.2W0.2)Si2, J. Mater. 5 (2019) 337–343, https://doi.org/10.1016/j.jmat.2019.03.002.

[22] J. Gild, Y. Zhang, T. Harrington, S. Jiang, T. Hu, M.C. Quinn, W.M. Mellor, N. Zhou, K. Vecchio, J. Luo, High-entropy metal diborides: a new class of high-entropy materials and a new type of ultrahigh temperature ceramics, Sci. Rep. 6 (2016) 2–11, https://doi.org/10.1038/srep37946.

[23] R. Mitra, A. Bajpai, K. Biswas, Machine learning based approach for phase prediction in high entropy borides, Ceram. Int. 48 (2022) 16695–16706, https://doi.org/10.1016/j.ceramint.2022.02.218.

[24] L. Feng, F. Monteverde, W.G. Fahrenholtz, G.E. Hilmas, Superhard high-entropy AlB2-type diboride ceramics, Scripta Mater. 199 (2021) 113855, https://doi.org/10.1016/j.scriptamat.2021.113855.

[25] X. Zhang, W. Li, S. Wan, J. Feng, M. Song, J. Liu, G. Wang, Z. Chen, B. Chen, H. Zhang, Pressure dependence of the electrical conductivities of high-entropy diborides, J. Eur. Ceram. Soc. 42 (2022) 6951–6957, https://doi.org/10.1016/j.jeurceramsoc.2022.08.007.

[26] Y. Gao, L. Huang, Z. Tong, J. Liu, Q. Zhang, H. Zhang, Q. Jia, S. Zhang, Low-temperature synthesis of high-entropy (Hf0.2Ti0.2Mo0.2Ta0.2Nb0.2)B2 powders combined with theoretical forecast of its elastic and thermal properties, J. Am. Ceram. Soc. 105 (2022) 6370–6383, https://doi.org/10.1111/jace.18596.

[27] W. Qi, B. Chen, X. Yang, N. Liu, Z. Jia, W. Wang, Phase stability, mechanical and thermodynamic properties of (Hf, Zr, Ta, M)B2 (M= Nb, Ti, Cr, W) quaternary high-entropy diboride ceramics via first-principles calculations, Ceram. Int. 49 (2023) 33255–33264, https://doi.org/10.1016/j.ceramint.2023.08.034.

[28] L. Feng, W.G. Fahrenholtz, G.E. Hilmas, S. Curtarolo, Boro/carbothermal reduction co-synthesis of dual-phase high-entropy boride-carbide ceramics, J. Eur. Ceram. Soc. 43 (2023) 2708–2712, https://doi.org/10.1016/j.jeurceramsoc.2022.12.056.

[29] G. Tallarita, R. Licheri, S. Garroni, S. Barbarossa, R. Orrù, G. Cao, High-entropy transition metal diborides by reactive and non-reactive spark plasma sintering: a comparative investigation, J. Eur. Ceram. Soc. 40 (2020) 942–952, https://doi.org/10.1016/j.jeurceramsoc.2019.10.031.

[30] J. Liu, X. Shen, Y. Wu, F. Li, Y. Liang, G. Zhang, Mechanical properties of hot-pressed high-entropy diboride-based ceramics, J. Adv. Ceram. 9 (2020) 503–510, https://doi.org/10.1007/s40145-020-0383-8. CN 10-1154/TQ.

[31] R.F. Guo, H.R. Mao, P. Shen, Ultra-fast high-temperature synthesis and densification of high-entropy diborides and diboride-carbide ceramics, J. Eur. Ceram. Soc. 43 (2023) 5763–5773, https://doi.org/10.1016/j.jeurceramsoc.2023.05.042.

[32] Y. Zhang, S.K. Sun, W. Zhang, Y. You, W.M. Guo, Z.W. Chen, J.H. Yuan, H.T. Lin, Improved densification and hardness of high-entropy diboride ceramics from fine powders synthesized via borothermal reduction process, Ceram. Int. 46 (2020) 14299–14303, https://doi.org/10.1016/j.ceramint.2020.02.214.

[33] A.C. Feltrin, F. Akhtar, High-temperature oxidation kinetics of a metastable dual-phase diboride and a high-entropy diboride, J. Eur. Ceram. Soc. 43 (2023) 7363–7372, https://doi.org/10.1016/j.jeurceramsoc.2023.08.001.

[34] P. Peng, J.X. Liu, J. Song, Y. Liang, G.J. Zhang, High-entropy diboride ceramics with graphite addition, J. Eur. Ceram. Soc. 44 (2023) 2695–2703, https://doi.org/10.1016/j.jeurceramsoc.2023.12.042.

[35] Z. Yang, Y. Gong, S. Zhang, X. Lv, J. Hu, G. Zhang, G. Yu, S. Song, Microstructure and properties of high-entropy diboride composites prepared by pressureless sintering, J. Alloys Compd. 952 (2023) 169975, https://doi.org/10.1016/j.jallcom.2023.169975.

[36] M.S. Bin Hoque, M. Milich, M.S. Akhanda, S. Shivakumar, E.R. Hoglund, D. Staicu, M. Qin, K.F. Quiambao-Tomko, J.A. Tomko, J.L. Braun, J. Gild, D.H. Olson, K. Aryana, Y.R. Koh, R. Galib, L. Vlahovic, D. Robba, J.T. Gaskins, M. Zebarjadi, J. Luo, P.E. Hopkins, Thermal and ablation properties of a high-entropy metal diboride: (Hf0.2Zr0.2Ti0.2Ta0.2Nb0.2)B2, J. Eur. Ceram. Soc. 43 (2023) 4581–4587, https://doi.org/10.1016/j.jeurceramsoc.2023.03.065.

[37] V.I. Ivashchenko, V.I. Shevchenko, L.A. Ivashchenko, L. Gorb, J. Leszczynski, Comparative first-principles study of the (TiZrHfNbTa)B2 high entropy solid solution and its constituent binary diborides, Comput. Condens. Matter. 33 (2022) e00762, https://doi.org/10.1016/j.cocom.2022.e00762.

[38] Y. Yang, Y. Bi, K. Sun, L. Qiao, G. Liang, H. Wang, J. Yuan, Y. Chen, The effect of chemical element on hardness in high-entropy transition metal diboride ceramics, J. Eur. Ceram. Soc. (2023) 1–8, https://doi.org/10.1016/j.jeurceramsoc.2023.06.003.

[39] İ. Süzer, Y.E. Özçakıcı, A.S. Tekinşen, K.G. Bayrak, S. Mertdinç-Ülküseven, Ö. Balcı-Çağıran, M.L. Öveçoğlu, D. Ağaoğulları, High entropy (HfTiZrVNb)B2 ceramic particulate reinforced Al matrix composites: synthesis, mechanical, microstructural

and thermal characterization, Ceram. Int. 50 (2024) 26583–26595, https://doi.org/10.1016/j.ceramint.2024.04.386.

[40] B. Wang, X. Li, Y.X. Wang, Y.F. Tu, Phase stability and physical properties of manganese borides: a first-principles study, J. Phys. Chem. C 115 (2011) 21429–21435, https://doi.org/10.1021/jp2073683.

[41] M. Qin, J. Gild, H. Wang, T. Harrington, K.S. Vecchio, J. Luo, Dissolving and stabilizing soft WB2 and MoB2 phases into high-entropy borides via boron-metals reactive sintering to attain higher hardness, J. Eur. Ceram. Soc. 40 (2020) 4348–4353, https://doi.org/10.1016/j.jeurceramsoc.2020.03.063.

[42] J. Gild, A. Wright, K. Quiambao-Tomko, M. Qin, J.A. Tomko, M. Shafkat bin Hoque, J.L. Braun, B. Bloomfield, D. Martinez, T. Harrington, K. Vecchio, P. E. Hopkins, J. Luo, Thermal conductivity and hardness of three single-phase high-entropy metal diborides fabricated by borocarbothermal reduction and spark plasma sintering, Ceram. Int. 46 (2020) 6906–6913, https://doi.org/10.1016/j.ceramint.2019.11.186.

[43] M. Qin, J. Gild, C. Hu, H. Wang, M.S. Bin Hoque, J.L. Braun, T.J. Harrington, P. E. Hopkins, K.S. Vecchio, J. Luo, Dual-phase high-entropy ultra-high temperature ceramics, J. Eur. Ceram. Soc. 40 (2020) 5037–5050, https://doi.org/10.1016/j.jeurceramsoc.2020.05.040.

[44] Y. Zhang, W.M. Guo, Z. Bin Jiang, Q.Q. Zhu, S.K. Sun, Y. You, K. Plucknett, H. T. Lin, Dense high-entropy boride ceramics with ultra-high hardness, Scripta Mater. 164 (2019) 135–139, https://doi.org/10.1016/j.scriptamat.2019.01.021.

[45] Y. Zhang, Z. Bin Jiang, S.K. Sun, W.M. Guo, Q.S. Chen, J.X. Qiu, K. Plucknett, H. T. Lin, Microstructure and mechanical properties of high-entropy borides derived from boro/carbothermal reduction, J. Eur. Ceram. Soc. 39 (2019) 3920–3924, https://doi.org/10.1016/j.jeurceramsoc.2019.05.017.

[46] Y. Zhang, S.K. Sun, W.M. Guo, W. Zhang, L. Xu, J.H. Yuan, D.K. Guan, D.W. Wang, Y. You, H.T. Lin, Fabrication of textured (Hf0.2Zr0.2Ta0.2Cr0.2Ti0.2)B2 high-entropy ceramics, J. Eur. Ceram. Soc. 41 (2021) 1015–1019, https://doi.org/10.1016/j.jeurceramsoc.2020.08.071.

[47] D. Demirskyi, T.S. Suzuki, K. Yoshimi, O. Vasylkiv, Synthesis of medium-entropy (Zr1/3Hf1/3Ta1/3)B2 using the spark plasma consolidation of diboride powders, J. Ceram. Soc. Japan. 128 (2020) 977–980, https://doi.org/10.2109/jcersj2.20151.

[48] W. Yang, G. Xiao, Z. Ren, Spark plasma sintering synthesis of ReB2-type medium-entropy diboride (W1/3Re1/3Ru1/3)B2 with high hardness, Scripta Mater. 227 (2023) 115299, https://doi.org/10.1016/j.scriptamat.2023.115299.

[49] Z. Zhang, S. Zhu, Y. Liu, L. Liu, Z. Ma, Phase structure, mechanical properties and thermal properties of high-entropy diboride (Hf0.25Zr0.25Ta0.25Sc0.25)B2, J. Eur. Ceram. Soc. 42 (2022) 5303–5313, https://doi.org/10.1016/j.jeurceramsoc.2022.05.066.

[50] A.C. Murchie, J.L. Watts, W.G. Fahrenholtz, G.E. Hilmas, Room-temperature mechanical properties of a high-entropy diboride, Int. J. Appl. Ceram. Technol. 19 (2022) 2293–2299, https://doi.org/10.1111/ijac.14026.

[51] J.W. Yeh, Alloy design strategies and future trends in high-entropy alloys, Jom 65 (2013) 1759–1771, https://doi.org/10.1007/s11837-013-0761-6.

[52] S.M. Smith, W.G. Fahrenholtz, G.E. Hilmas, Pressureless sintering of high-entropy boride ceramics, J. Eur. Ceram. Soc. 43 (2023) 5168–5173, https://doi.org/10.1016/j.jeurceramsoc.2023.04.050.

[53] Q.Q. Zhu, Z. Zhang, Y. Zhang, Q.Y. Liu, B.C. Song, W.M. Guo, H.T. Lin, Effects of TaB2 and TiB2 on the grain growth behavior and kinetics of HfB2 ceramics during pressureless sintering, J. Am. Ceram. Soc. 103 (2020) 3330–3337, https://doi.org/10.1111/jace.16980.

[54] Y. Zhang, L. Shan, Y.F. Chai, W.M. Guo, T.Q. Zhang, L. Xu, J.L. Cong, H.T. Lin, L. Y. Wei, W.M. Ma, Influence of Cr content on sintering, textured structure, and properties of (Hf, Zr, Ta, Cr, Ti)B2 high-entropy boride ceramics, Ceram. Int. 49 (2023) 16029–16037, https://doi.org/10.1016/j.ceramint.2023.01.200.

[55] A. Eldesouky, M. Johnsson, H. Svengren, M.M. Attallah, H.G. Salem, Effect of grain size reduction of AA2124 aluminum alloy powder compacted by spark plasma sintering, J. Alloys Compd. 609 (2014) 215–221, https://doi.org/10.1016/j.jallcom.2014.04.136.

[56] R. Daly, M. Khitouni, N. Njeh, Effect of high energy mechanical milling on the properties of CuA 1 copper, Phys. Procedia 2 (2009) 685–691, https://doi.org/10.1016/j.phpro.2009.11.011.

[57] B. Duan, Y. Yu, X. Liu, D. Wang, Z. Wu, A novel non-equiatomic (W35ta35mo15nb15)95ni5 refractory high entropy alloy with high density

fabricated by powder metallurgical process, Metals 10 (2020) 1–13, https://doi.org/10.3390/met10111436.

[58] M. Qin, Q. Yan, Y. Liu, J. Luo, A new class of high-entropy M3B4 borides, J. Adv. Ceram. 10 (2021) 166–172, https://doi.org/10.1007/s40145-020-0438-x. CN 10-1154/TQ.

[59] Y. Yang, J. Bi, K. Sun, L. Qiao, Y. Liu, Y. Li, H. Wang, Y. Liang, M. Shang, Novel (Hf0.2Zr0.2Ta0.2V0.2Nb0.2)B2 high entropy diborides with superb hardness sintered by SPS under a mild condition, Ceram. Int. 48 (2022) 30859–30867, https://doi.org/10.1016/j.ceramint.2022.07.040.

[60] J. Gu, J. Zou, S.K. Sun, H. Wang, S.Y. Yu, J. Zhang, W. Wang, Z. Fu, Dense and pure high-entropy metal diboride ceramics sintered from self-synthesized powders via boro/carbothermal reduction approach, Sci. China Mater. 62 (2019) 1898–1909, https://doi.org/10.1007/s40843-019-9469-4.

[61] C. Oses, C. Toher, S. Curtarolo, High-entropy ceramics, Nat. Rev. Mater. 5 (2020) 295–309, https://doi.org/10.1038/s41578-019-0170-8.

[62] W. Gong, T. Wang, W. Luo, Y. Du, L. Ye, R. Song, H. Cui, T. Zhao, W. Yang, Z. Dai, Y. Hong, Synthesis and characterization of high-purity, high-entropy diboride ceramic powders by a liquid phase method, Materials 16 (23) (2023) 7431, https://doi.org/10.3390/ma16237431.

[63] B. Storr, L. Moore, K. Chakrabarty, Z. Mohammed, V. Rangari, C.C. Chen, S. A. Catledge, Properties of high entropy borides synthesized via microwave-induced plasma, Apl. Mater. 10 (2022), https://doi.org/10.1063/5.0098276.

[64] L. Qiao, Y. Liu, Y. Gao, J. Bi, Y. Li, C. Liu, J. Gao, W. Wang, Z. Qian, First-principles prediction, fabrication and characterization of (Hf0.2Nb0.2Ta0.2Ti0.2Zr0.2)B2 high-entropy borides, Ceram. Int. 48 (2022) 17234–17245, https://doi.org/10.1016/j.ceramint.2022.02.281.

[65] S. Barbarossa, R. Orrù, V. Cannillo, A. Iacomini, S. Garroni, M. Murgia, G. Cao, Fabrication and characterization of quinary high entropy-ultra-high temperature diborides, Ceramics 4 (2021) 108–120, https://doi.org/10.3390/ceramics4020010.

[66] S. Barbarossa, R. Orrù, S. Garroni, R. Licheri, G. Cao, Ultra high temperature high-entropy borides: effect of graphite addition on oxides removal and densification behaviour, Ceram. Int. 47 (2021) 6220–6231, https://doi.org/10.1016/j.ceramint.2020.10.200.

[67] H. Chen, H. Xiang, F.Z. Dai, J. Liu, Y. Zhou, Porous high entropy (Zr0.2Hf0.2Ti0.2Nb0.2Ta0.2)B2: a novel strategy towards making ultrahigh temperature ceramics thermal insulating, J. Mater. Sci. Technol. 35 (2019) 2404–2408, https://doi.org/10.1016/j.jmst.2019.05.059.

[68] C.A. Schneider, W.S. Rasband, K.W. Eliceiri, NIH Image to ImageJ: 25 years of image analysis, Nat. Methods 9 (2012) 671–675, https://doi.org/10.1038/nmeth.2089.

[69] A.R. Smith, A Pixel Is Not a Little Square, Pixar Tech. Memo, 1995, pp. 1–11.

[70] F. Li, R. Hu, H. Yu, J. Yang, Application of ImageJ in the rock thin section image analysis: the separation and quantitative calculation of crystal-glass two phases, SDRP J, Earth Sci. Environ. Stud. 4 (2019) 609–616, https://doi.org/10.25177/jeses.4.3.ra.502.

[71] F. Zeitvogel, G. Schmid, L. Hao, P. Ingino, M. Obst, ScatterJ: an ImageJ plugin for the evaluation of analytical microscopy datasets, J. Microsc. 261 (2016) 148–156, https://doi.org/10.1111/jmi.12187.

[72] K.C. Polavaram, N. Garg, High-fidelity and high-resolution phase mapping of granites via confocal Raman imaging, Sci. Rep. 11 (2021) 1–10, https://doi.org/10.1038/s41598-021-87488-1.

[73] M. Ender, J. Joos, T. Carraro, E. Ivers-Tiffée, Three-dimensional reconstruction of a composite cathode for lithium-ion cells, Electrochem. Commun. 13 (2011) 166–168, https://doi.org/10.1016/j.elecom.2010.12.004.

[74] M. Ender, J. Joos, T. Carraro, E. Ivers-Tiffée, Quantitative characterization of LiFePO 4 cathodes reconstructed by FIB/SEM tomography, J. Electrochem. Soc. 159 (2012) A972–A980, https://doi.org/10.1149/2.033207jes.

[75] D. Sage, L. Donati, F. Soulez, D. Fortun, G. Schmit, A. Seitz, R. Guiet, C. Vonesch, M. Unser, DeconvolutionLab2: an open-source software for deconvolution microscopy, Methods 115 (2017) 28–41, https://doi.org/10.1016/j.ymeth.2016.12.015.

[76] Y. Zhou, H. Xiang, Z. Feng, Z. Li, General trends in electronic structure, stability, chemical bonding and mechanical properties of ultrahigh temperature ceramics TMB2 (TM=transition metal), J. Mater. Sci. Technol. 31 (2015) 285–294, https://doi.org/10.1016/j.jmst.2014.09.014.